Bioorganic & Medicinal Chemistry 18 (2010) 2304–2316

Contents lists available at ScienceDirect

Bioorganic & Medicinal Chemistry

journal homepage: www.elsevier.com/locate/bmc

Pharmacophore modeling, resistant mutant isolation, docking, and MM-PBSA analysis: Combined experimental/computer-assisted approaches to identify new inhibitors of the bovine viral diarrhea virus (BVDV)

Michele Tonelli [a], Vito Boido [a], Paolo La Colla [b], Roberta Loddo [b], Paola Posocco [c], Maria Silvia Paneni [c], Maurizio Fermeglia [c], Sabrina Pricl [c,*]

[a] Deparment of Pharmaceutical Sciences, University of Genoa, Viale Benedetto XV 3, 16132 Genova, Italy
[b] Department of Biomedical Sciences and Technologies, University of Cagliari, Cittadella Universitaria, 09042 Monserrato (Cagliari), Italy
[c] Molecular Simulation Engineering (MOSE) Laboratory, Department of Chemical, Environmental, and Raw Materials Engineering, University of Trieste, Piazzale Europa 1, 34127 Trieste, Italy

ARTICLE INFO

Article history:
Received 15 September 2009
Revised 20 January 2010
Accepted 22 January 2010
Available online 29 January 2010

Keywords:
Anti-BVDV agents
2-Phenylbenzimidazoles
Molecular modeling
BVDV resistant mutants

ABSTRACT

Starting from a series of our new 2-phenylbenzimidazole derivatives, shown to be selectively and potently active against the bovine viral diarrhea virus (BVDV), we developed a hierarchical combined experimental/molecular modeling strategy to explore the drug leads for the BVDV RNA-dependent RNA-polymerase. Accordingly, a successful 3D pharmacophore model was developed, characterized by distinct chemical features that may be responsible for the activity of the inhibitors. BVDV mutants resistant to lead compounds in our series were then isolated, and the mutant residues on the viral molecular target, the RNA-dependent RNA-polymerase, were identified. Docking procedures upon pharmacophoric constraints and mutational data were carried out, and the binding affinity of all active compounds for the RdRp were estimated. Given the excellent agreement between in silico and in vitro data, this procedure is currently being employed in the design a new series of more selective and potent BVDV inhibitors.

1. Introduction

The Flaviviridae family, well known human and animal population pathogens, contains viruses with single-stranded positive-sense RNA genomes (ssRNA$^+$), and comprises three genera and several viruses that are currently unassigned to specific genera. The *Hepacivirus* genus includes the hepatitis C virus (HCV). Viruses such as GB virus-A and GB virus-A-like agents, GB virus-D and GBV-C or hepatitis G virus, while at present not formally classified within the *Hepacivirus* genus, are closely related to HCV and represent unassigned members of Flaviviridae. This family also comprises the *Flavivirus* genus, with viruses such as Dengue Fever (DFV), Yellow Fever (YFV), West Nile (WN), Japanese encephalitis (JEV), and tick-borne encephalitis (TBEV), and the *Pestivirus* genus, which includes bovine viral diarrhea (BVDV), Border Disease (BDV), and Classical Swine Fever (CSFV) viruses.

Flaviviruses are important human pathogens prevalent throughout the world, and cause a range of acute febrile illness and encephalitic and hemorrhagic diseases. Although an effective vaccine against YFV has been available since the late 1930s, utilization is incomplete in many areas.[1]

HCV is a major cause of human hepatitis, globally.[2] The World Health Organization (WHO) estimates that over 170 million people worldwide, ~3% of the world's population, are presently infected with this virus.[3,4] Moreover, most infections become persistent, and there is a compelling evidence that, within 10–20 years, these chronic infections progress towards cirrhosis and then to hepatocarcinoma in about 20% and 5%, respectively.[5,6] To date, there is no vaccine available against HCV. Furthermore, the sole currently available therapy (pegylated interferon in combination with ribavirin) is expensive, with limited efficacy (50–60% of patient treated) and is often associated with severe and adverse events.[7,8] The development of new, effective antiviral compounds for combating this debilitating human pathogen is therefore of paramount importance, and is currently an intensive area of pharmaceutical research.[9]

Pestivirus infections of domesticated livestock cause significant economic losses worldwide. These viruses cause a range of clinical manifestations including abortion, teratogenesis, respiratory problems, chronic wasting disease, immune system dysfunction and predisposition to secondary viral and bacterial infections. BVDV, the prototype of the *Pestivirus* genus of the Flaviviridae family and a major pathogen of cattle, can also establish a persistent infection (PI) in animals that remain viremic throughout life and serve as continuous virus reservoirs.[10] Persistently infected

* Corresponding author. Tel.: +39 040 5583750; fax: +39 040 569823.
E-mail address: sabrina.pricl@dicamp.units.it (S. Pricl).

0968-0896/$ - see front matter © 2010 Elsevier Ltd. All rights reserved.
doi:10.1016/j.bmc.2010.01.058

animals often succumb to fatal mucosal disease. Furthermore, BVDV shows the ability to cross the placenta of susceptible animals causing a variety of fetal infections.[11] For the United States alone, this has been estimated to translate approximately into a loss of $10 to 40 million for million calves. These losses are projected into reduced milk production, limited reproductive performance, growth retardation, and increased mortality among young stocks.[12] CSFV also represents a cause for major economic losses, especially in those countries with industrialized pig breeding.[13] Notwithstanding the accessibility to vaccines against BVDV and CSFV, and the implementation of massive eradication or control programs,[14] both viruses still constitute a serious, agronomical burden. Accordingly, although not likely suited to treat large herds, the availability of antiviral agents that specifically and selectively inhibit the replication of these viruses might contribute substantially to control the viral outbreaks. For example, since protection after vaccination becomes effective from 10 to 14 days later, antiviral treatment following vaccination may result in almost immediate protection against infection, thus preventing further virus transmission and avoiding large-scale culling of healthy animals.

Notably, BVDV is also still considered to be a valuable surrogate virus for HCV virus.[15] Indeed, in some aspects of viral replication, BVDV is more advantageous in comparison to the currently used HCV replicon system,[16] as the latter does not undergo a complete replication cycle. Hence, the early stages (e.g., vital attachment, entry, and uncoating) and late stages (virion assembly and release) of the viral replication cycle cannot be studied in the HCV replicon system. Although very recently, robust and efficient HCV cell culture systems have been described in the literature,[17] important insight into the mechanism of antiviral activity of anti-*Pestivirus* compounds may provide valuable information for the design of novel antiviral strategies against HCV.[15,18]

Recently, as part of a large program of design, synthesis, in silico, and in vitro screening of new classes of non-nucleoside inhibitors of BVDV (as a surrogate for HCV), we reported the synthesis of 76 2-phenylbenzimidazole derivatives, 31 of which were found to elicit specific antiviral activity against BVDV (Scheme 1, Tables 1–3).[19]

Interestingly, the EC_{50} values for 22 of these compounds were determined in the sub/micromolar range (0.8–10 μM) and, hence, are in accordance with those required for needs suitable for pharmaceutical development. Further, three compounds endowed with the highest activity and lowest toxicity (as essayed against host cells MDBK and human cells MT-4) were also shown to target the RNA-dependent RNA-polymerase of BVDV, by inhibiting the enzyme activity again in the low micromolar range (IC_{50} = 3–18 μM).[19]

In order to find a molecular rationale for the mechanism by which our compounds could inhibit the BVDV RdRp, and to develop a predictive tool for the design of a second generation of more potent and selective inhibitors, we developed a hierarchical, combined computational/experimental procedure which included the sequential application of four steps: (1) pharmacophore modeling; (2) experimental isolation of BVDV mutants resistant to the most active compounds; (3) molecular docking based upon information obtained at points (1) and (2); and (4) molecular-mechanics/Poisson–Boltzmann/surface area (MM/PBSA) calculations to estimate the binding affinities of the compounds to the target enzyme.

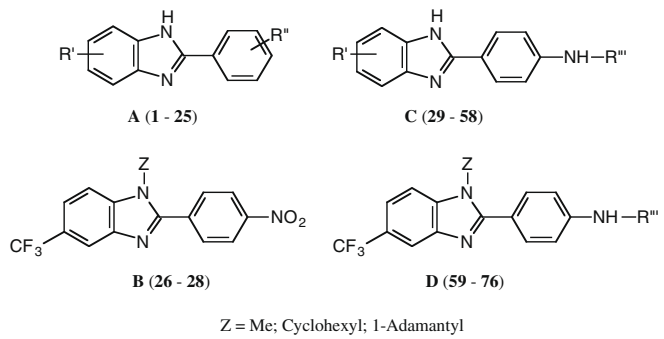

Scheme 1. Structures of the 76 2-phenylbenzimidazole derivatives considered in this work. The structural details of the entire compound series is given in Table 1.

2. 3D pharmacophore modeling

A three-dimensional pharmacophore model captures the three-dimensional arrangement of the structural features shared by all active molecules that are presumably essential for the desired pharmacological activity. The HypoGen algorithm of CATALYST[20] allows a maximum of five features to be present in the pharmacophore generation process. Accordingly, from the 11 features available in the CATALYST features dictionary (see Section 7 for details), we excluded *a priori* all those that clearly did not match the chemistry of the molecules of the training set (e.g., negative charge (NC) sites). Also, preliminary runs including hydrogen bond acceptor lipid (HBAl), the hydrophobic aliphatic (HYAl) and the more generic hydrophobic feature (HY) confirmed that these features were never used in the generation of the pharmacophore models. Thus, all these features were removed from the list. In summary, the following five chemical features were taken into account for hypothesis generation with HypoGen: hydrogen bond acceptor (HBA), hydrogen bond donor (HBD), hydrophobic aromatic (HYAr), ring aromatic (Ar), and positive ionizable (PI).

A total of 10 hypotheses were generated by the HypoGen algorithm, all characterized by the same three features: HBA, HBD, and HYAr, as shown in Table 4. The total hypothesis cost of these ten best models varies between 100.1 for the best ranked model (Hypo1) to 108.4 for the lowest ranked one (Hypo10). Such a confined difference (eight bits) reflects both the homogeneity of the generated hypotheses and the adequacy of the molecular training set. The difference between the null and the fixed costs, which should be higher than 70 to guarantee a robust correlation, is 96 in our case. This corresponds to a chance of true correlation in the data greater than 90%.[21] Further, the evidence that, for all hypotheses the total costs are much closer to the fixed cost (94.8) than to the null cost (196.3) also constitutes an indication that meaningful models are obtained. As reported in Table 4, for Hypo 1 the configurational cost value is equal to 13.9, which is well below the threshold value of 17. Finally, the root-mean-square deviations (RMSD) and the correlation coefficients (ρ) between estimated and experimental affinities range from 0.6 to 0.8, and from 0.98 to 0.90, respectively. Considering that all the generated pharmacophores map the molecules of the training set in a similar way, the first model (Hypo1), characterized by the highest cost difference, the lowest RMDS, and the best ρ values was selected for further analysis.

The affinities of the 22 compounds in the training set estimated using Hypo1 are reported in Table 5, along with the experimental values and the relevant errors (expressed as the ratio between estimated and experimental values). This Table clearly shows that all activities were well predicted, all errors being mostly below 1.5 and, however, below a maximum value of 3. Figures 1A–C, illustrate the selected Hypo1 pharmacophore model, while Figure 1D–F show the mapping of compounds **51**, **53**, and **27** onto Hypo1, respectively. As can be seen from Figure 1D and E, in both **51** and **53** the aromatic ring of the benzimidazole moiety matches the HYAr feature, whilst the carbonyl group and one nitrogen atom of the azole ring nicely map the HBA and HBD functions, respec-

Table 1
Antiviral activity[19] of 2-phenylbenzimidazole derivatives of structure **A** (**1**–**25**) and **B** (**26**–**28**)

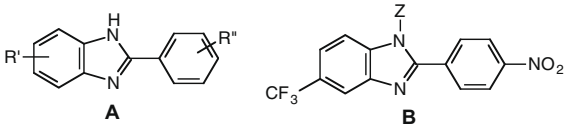

Compound	R′	R″	BVDV EC_{50}[a] (μM)	Compound	R′	R″	BVDV EC_{50}[a] (μM)
1	H	2-NO_2	>100	**15**	5-CF_3	2,6-DiF	>100
2	H	2,4-DiNO_2	>20	**16**	5-NO_2	2,4-DiOCH_3	45
3	5-CF_3	4-OH	>51	**17**	5-NO_2	2,3,4-TriOCH_3	>100
4	5-CF_3	4-OCH_3	1	**18**	5-$COCH_3$	2,4-DiOCH_3	42
5	5-CF_3	3-OCH_3	>28	**19**	5-$COCH_3$	2,3,4-TriOCH_3	>100
6	5-CF_3	2,4-DiOCH_3	>100	**20**	5,6-DiCl	4-OH	>11
7	5-CF_3	3,5-DiOCH_3	>100	**21**	5,6-DiCl	4-OCH_3	>2.5
8	5-CF_3	2,3,4-TriOCH_3	>100	**22**	5,6-DiCl	2-NO_2,4-OCH_3	>28
9	5-CF_3	3,4,5-TriOCH_3	>18	**23**	5,6-DiCl	2-NH_2,4-OCH_3	>6.5
10	5-CF_3	2-NO_2,4-OCH_3	>55	**24**	5,6-DiCl	4-NO_2	>56
11	5-CF_3	2-NH_2,4-OCH_3	>4	**25**	5,6-DiCl	2,6-DiF	>43
12	5-CF_3	4-NO_2	>6	**26**[b]	5-CF_3	4-NO_2	>100
13	5-CF_3	2,4-DiNO_2	>16	**27**[c]	5-CF_3	4-NO_2	60
14	5-CF_3	4-F	>19	**28**[d]	5-CF_3	4-NO_2	>100

[a] Compound concentration (μM) required to achieve 50% protection of MDBK cells from BVDV (bovine viral diarrhea virus) induced cytopathogenicity, as determined by the MTT method.[19]
[b] Z = methyl.
[c] Z = cyclohexyl.
[d] Z = 1-adamantyl.

Table 2
Antiviral activity[19] of 2-phenylbenzimidazole derivatives of structure **C** (**29**–**58**)

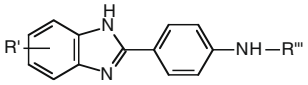

Compound	R′	R‴	BVDV EC_{50}[a] (μM)	Compound	R′	R‴	BVDV EC_{50}[a] (μM)
29	H	H	16	**44**	5-CF_3	$O(CH_2CH_2)_2N–CH_2CO$	>100
30	H	CH_3CO	90	**45**	5-CF_3	$S(CH_2CH_2)_2N–CH_2CO$	>100
31	H	CH_3CH_2CO	47	**46**	5-CF_3	$C_6H_5N(CH_2CH_2)_2N–CH_2CO$	>32
32	H	$(CH_2)_4N–CH_2CO$	10	**47**	5-CF_3	Homolupinanoyl	2
33	H	$(CH_2)_5N–CH_2CO$	7	**48**	5-CF_3	$HOOC(CH_2)_2CO$	>100
34	H	$O(CH_2CH_2)_2N–CH_2CO$	>77	**49**	5-CF_3	4-(5-CF_3-benzimidazol-2-yl)phenylcarbamoyl	>100
35	H	Homolupinanoyl	10	**50**	5-NO_2	H	1.5
36	5-CF_3	H	15	**51**	5-NO_2	CH_3CO	0.8
37	5-CF_3	CH_3CO	1.3	**52**	5,6-DiCl	H	1
38	5-CF_3	CH_3CH_2CO	>100	**53**	5,6-DiCl	CH_3CO	1
39	5-CF_3	$ClCH_2CO$	>17	**54**	5,6-DiCl	$(CH_2)_4N–CH_2CO$	2.5
40	5-CF_3	1-Adamantyl-NH–CH_2CO	>23	**55**	5,6-DiCl	$(CH_2)_5N–CH_2CO$	2
41	5-CF_3	$(C_2H_5)_2N–CH_2CO$	2	**56**	5,6-DiCl	$O(CH_2CH_2)_2N–CH_2CO$	2.4
42	5-CF_3	$(CH_2)_4N–CH_2CO$	3	**57**	5,6-DiCl	$O(CH_2CH_2)_2N–CH_2CO$	>100
43	5-CF_3	$(CH_2)_5N–CH_2CO$	2	**58**	5,6-DiCl	$CH_3N(CH_2CH_2)_2N–CH_2CO$	4

[a] Compound concentration (μM) required to achieve 50% protection of MDBK cells from BVDV (Bovine Viral Diarrhea Virus) induced cytopathogenicity, as determined by the MTT method.[19]

tively. The estimated affinities for **51** and **53** are 0.4 μM and 1.1 μM, while the corresponding experimental affinities are 0.8 μM and 1 μM, respectively.

Figure 1F is an example of a pharmacophore mapping of a compound that is less active than the former two. Compound **27** does not map all the features encoded in Hypo1. In fact, **27** maps the HYAr function, again by means of the benzimidazole phenyl ring of the benzimidazole; however, it does not map both the remaining hydrogen bond features. According to this partial mapping, this compound is predicted to be less active.

To get additional confidence on the usefulness of the generated 3D pharmacophore, we validated the model by mapping a test set of 9 compounds (see Table 6). Indeed, a good correlation coefficient (0.88) was observed when a regression analysis was performed by mapping the test set onto the features of the best pharmacophore hypothesis Hypo1. The predicted and the experimental EC_{50} values for the test set along with the respective errors are given in Table 6. The average error in predicting the affinity of the test set molecules is 1; therefore, given the inherent simplicity of the pharmacophoric approach, and considering the intrinsic variability of the biological responses, we can conclude that the ability of the present 3D pharmacophore model in predicting the activity of these molecular series against BVDV is satisfactory. Figure 2 shows the mapping of one test set molecule (**33**) to Hypo1.

A second test was performed to check the statistical significance of 3D pharmacophore model Hypo1, based on a randomization pro-

Table 3
Antiviral activity[19] of 2-phenylbenzimidazole derivatives of structure **D** (**59–76**)

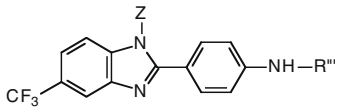

D

Compound	Z	R‴	BVDV EC_{50}[a] (μM)	Compound	Z	R‴	BVDV EC_{50}[a] (μM)
59	CH_3	H	69	**68**	CH_3	$C_6H_5N(CH_2CH_2)_2N–CH_2CO$	>1.4
60	CH_3	CH_3CO	>46	**69**	Cyclohexyl	H	>100
61	CH_3	CH_3CH_2CO	>100	**70**	Cyclohexyl	CH_3CO	>17
62	CH_3	$(C_2H_5)_2N–CH_2CO$	10	**71**	Cyclohexyl	CH_3CH_2CO	>18
63	CH_3	$(CH_2)_4N–CH_2CO$	7	**72**	1-Adamantyl	H	7
64	CH_3	$(CH_2)_5N–CH_2CO$	6	**73**	1-Adamantyl	CH_3CO	>82
65	CH_3	$O(CH_2CH_2)_2N–CH_2CO$	>100	**74**	1-Adamantyl	CH_3CH_2CO	>100
66	CH_3	$S(CH_2CH_2)_2N–CH_2CO$	8	**75**	1-Adamantyl	$ClCH_2CO$	>18
67	CH_3	$CH_3N(CH_2CH_2)_2N–CH_2CO$	15	**76**	1-Adamantyl	$C_6H_5N(CH_2CH_2)_2N–CH_2CO$	>100

[a] Compound concentration (μM) required to achieve 50% protection of MDBK cells from BVDV (Bovine Viral Diarrhea Virus) induced cytopathogenicity, as determined by the MTT method.[19]

Table 4
Ranking score, cost analysis (expressed in bits), and statistical parameters of the top 10 generated hypotheses using the training set BVDV inhibitors

Hypothesis	Total cost	Cost difference (null cost − total cost)	RMDS	ρ	Hypothesis	Total cost	Cost difference (null cost − total cost)	RMDS	ρ
1	100.1	96.2	0.630	0.982	**6**	105.2	91.1	0.729	0.921
2	101.8	94.5	0.652	0.967	**7**	106.3	90	0.744	0.917
3	102.5	93.8	0.689	0.960	**8**	107.6	88.7	0.769	0.912
4	103.4	92.9	0.692	0.945	**9**	108.1	88.2	0.786	0.904
5	104.7	91.6	0.705	0.932	**10**	108.4	87.9	0.808	0.901

Null cost: 196.3. Fixed cost: 94.8. Configurational cost: 13.9.

Table 5
Experimental and estimated activity values of the training set compounds used to develop pharmacophore hypothesis for BVDV inhibitors

Compound	Activity (μM)			Compound	Activity (μM)		
	Experimental	Estimated	Error[a]		Experimental	Estimated	Error[a]
51	0.8	0.4	−2.0	**54**	2.5	2.8	1.1
4	1.0	1.6	1.6	**42**	3.0	2.4	−1.3
52	1.0	3.0	3.0	**58**	4.0	3.2	−1.3
53	1.0	1.1	1.1	**62**	10	10	1.0
37	1.3	2.2	1.7	**36**	15	11	−1.4
50	1.5	1.1	−1.4	**29**	16	12	−1.3
41	2.0	2.6	1.3	**18**	42	41	1.0
43	2.0	2.4	1.2	**16**	45	50	1.1
47	2.0	4.3	2.2	**27**	60	55	−1.1
55	2.0	3.5	1.8	**59**	69	73	1.1
56	2.4	3.0	1.3	**30**	90	88	1.0

[a] Values in the error column represent the ratio of the estimated to experimental affinity, or its negative inverse if the ratio is less than one.

cedure derived from the Fisher method[22] using the CATSCRAMBLE program available in the CATALYST suite of programs. According to the validation procedure, the experimental affinities of the compounds in the training set were scrambled randomly, and the resulting new training set was used for a new HypoGen run. The parameters used in running these calculations were the same employed in the initial HypoGen calculations and, since a 98% confidence level was selected, 49 random hypothesis were generated. The resulting data clearly indicate that all values generated after randomization produced hypotheses with no predictive values. Indeed, none of the outcome hypotheses had lower cost score, better correlation or smaller root-mean-square deviation than the initial one. Table 7 lists the first 10 lowest total score values of the resulting 49 hypotheses for our test set molecules. In conclusion, there is a 98% chance for the best hypothesis to represent a true correlation in the training set affinity data for the present classes of compounds.

As a last, further statistical test, the *leave-one-out method*, which consists of re-computing the hypothesis by excluding from the training set one molecule at a time, was performed. Basically, this test aims at verifying whether the correlation is strongly dependent on one particular compound in the training set. The test is positive if the affinity of each excluded molecule is correctly predicted by the corresponding one-missing hypothesis. For each of the 21 new hypotheses generated according to this method we did not obtained meaningful differences between Hypo1 and each hypothesis resulting from the exclusion of one compound at a time, in terms of correlation coefficients, feature composition of the pharmacophore, and quality of the predicted affinity of the excluded molecule.

According to all evidences highlighted above, we believe that our in silico 3D pharmacophore model accounts for BVDV inhibitory activity of our set of 31 compounds and, despite its inherent

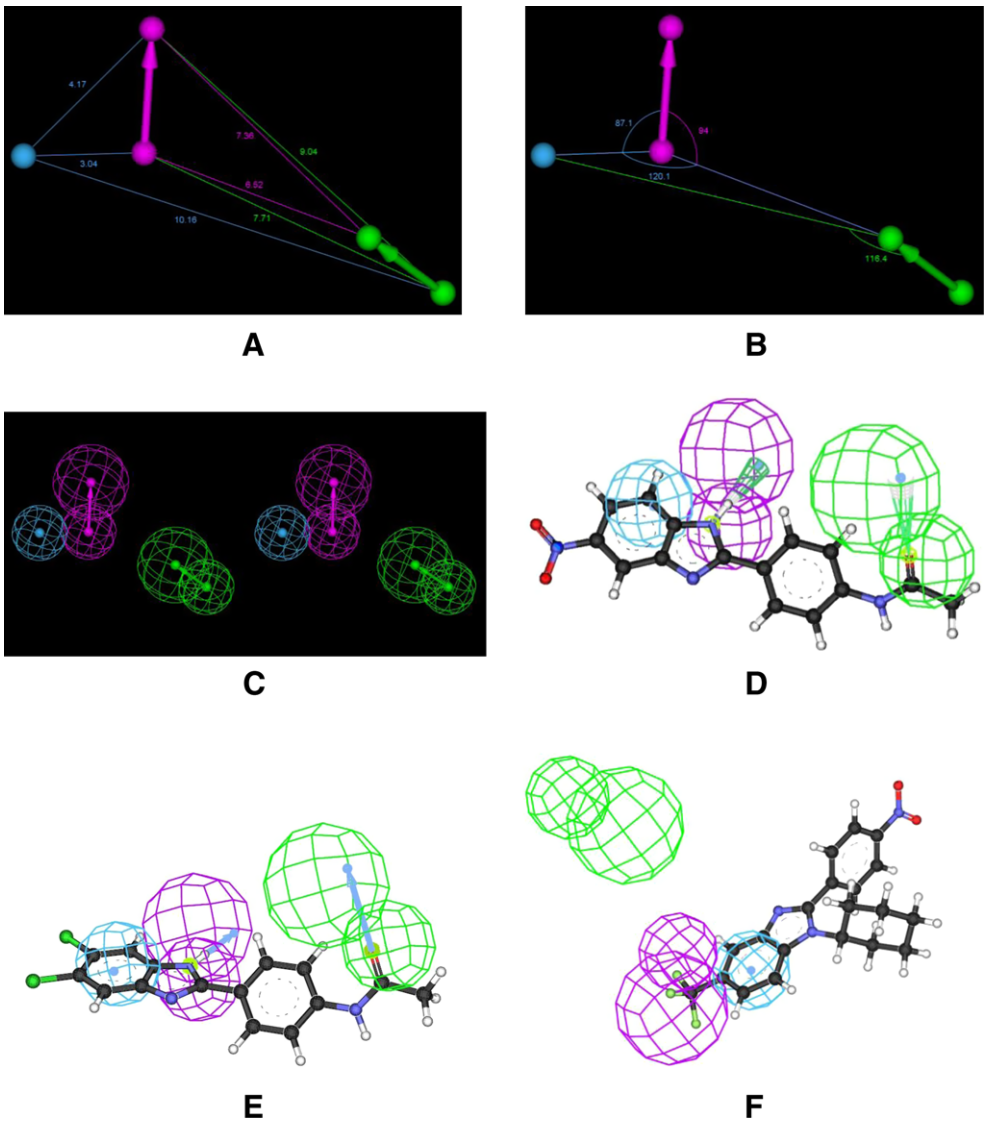

Figure 1. Geometrical relationships (A, B) among the features of the top-scoring pharmacophore Hypo1, parallel glaze stereo view of Hypo 1 (C), and pharmacophore mapping of compound **51** (D), **53** (E), and **27** (F) in the training set. The hypothesis features are portrayed as mashed spheres, color-coded as follows: light blue, HYAr; pink, HBD, light green, HBA. HBA and HBD are actually represented as a pair of spheres, the smaller sphere representing the location of the HBA atom on the ligand and the larger one the location of an HB donor on the receptor in the case of the HBA feature, and vice versa in the case of the NBD feature). Distances between features are given in Å, angles in °. Compounds are depicted as atom-colored sticks-and-balls: carbon, dark gray; oxygen, red; nitrogen, blue, hydrogen, white, chlorine, green.

Table 6
Experimental and estimated activity values of the test set compounds used to develop pharmacophore hypothesis for BVDV inhibitors

Compound	Activity (μM)			Compound	Activity (μM)		
	Experimental	Estimated	Error[a]		Experimental	Estimated	Error[a]
64	6.0	10	1.7	**32**	10	3.5	−2.9
33	7.0	4.0	−1.8	**35**	10	12	1.2
63	7.0	10	1.4	**67**	15	10	−1.5
72	7.0	11	1.6	**31**	47	48	1.0
66	8.0	5	−1.6				

[a] Values in the error column represent the ratio of the estimated to experimental affinity, or its negative inverse if the ratio is less than one.

simplicity, its predictive power is quite robust and can then be employed as a guide for discovering a possible binding site and for the successive docking of the inhibitors on their putative target enzyme, the BVDV RNA-dependent RNA-polymerase (RdRp).

3. Isolation of BVDV resistant mutants

BVDV, the best-studied *Pestivirus*, has a genome that consists of an approximately 12.6-kb positive-sense ssRNA. The BVDV genome is translated into a single polyprotein which is processed into at least four structural and six non-structural (NS) protein required for viral assembly and replication. Among the non-structural proteins, the NS5B is an RNA-dependent RNA-polymerase (RdRp) enzyme responsible for genome replication as a part of a larger, membrane associated replicase complex. In our previous work, we showed that the three compounds endowed with the most potent activity against wild-type BVDV in cell essays (**50**, **51**, and **53**) were also able to inhibit the viral RdRp in a dose-dependent, with

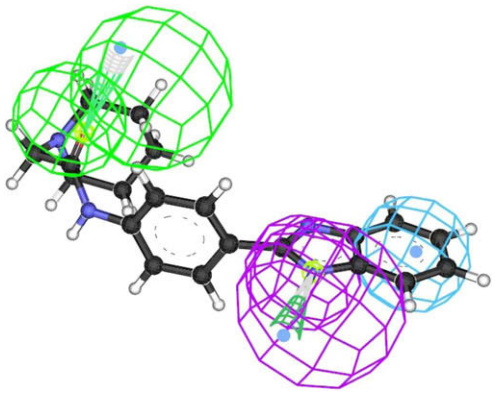

Figure 2. Pharmacophore mapping of compound **33** in the test set. Hypothesis features are color-coded as in Figure 2.

IC_{50} again in the low micromolar range.[19] Having ascertained the viral molecular target for our compounds, we then proceeded by isolating the corresponding drug-resistant viruses with a twofold purpose: (i) confirm the molecular target and, (ii) to locate the mutant position and use these information for driving the successive molecular docking operation (vide infra).

Compounds **50**^{R}, **51**^{R} and **53**^{R} BVDV viruses were selected by culturing wild-type BVDV in MDBK cells in the presence of increasing concentrations (up to 32 times the corresponding EC_{50} value) of the antiviral agents. As a result, when the genotypes of in vitro generated **50**^{R}, **51**^{R} and **53**^{R} viruses were determined, some mutations were detected at three different positions of the NS5B, that is, the gene that encodes the RdRp. No other mutations were found throughout the NS region of the drug-resistant virus genes. These positions, together with the corresponding wild-type/mutated residues and the concentrations at which drug-resistant viruses were isolated, are summarized in Table 8.

The three residues found mutated in the isolated drug-resistant BVDVs are located in the finger domain of the RdRp (vide infra). This region, in analogy with structurally-related HCV RdRp, is believed to play several critical roles in the enzyme activity, ranging from modulation of finger flexibility for template/product translocation, eventual dimerization of the RdRp in the replication complex, or protein–protein interactions, enabling the assembly of an active replication complex.[23] Also, quite interestingly, these amino acids locate in the close vicinity of F224, a residue previously reported as mutated in BVDV viruses resistant to highly selective inhibitors, for example, (3-[((2-dipropylamino)ethyl)thio]-5*H*-1,2,4-triazino[5,6-*b*]indole (VP32947)[24] and 5-[(4-bromophenyl)methyl]2-phenyl-5*H*-imidazo[4,5-*c*]pyridine (BPIP).[25]

4. Molecular docking onto the BVDV RdRp

The crystal structure of RdRp from several families of single- or double-strand RNA viruses, including BVDV,[26,27] have been recently made available in the Protein Data Bank (PDB) repository. As other RdRps, the crystal structures of this protein from BVDV presents the shape of a right hand with fingers, palm, and thumb domains.

In particular, the BVDV RNA-dependent RNA-polymerase core domain (residues 139–679) has a dimensions of approximately 74 × 60 × 58 Å around a central cavity,[26] which serves as for RNA template binding, nucleotides recruitment, and polymerization reaction. In addition, there is an N-terminal region (residues 71–138) of which residues 71–91 are disordered in the relevant crystal structure. A thorough search of a putative binding site for our molecules onto BVDV RdRp was conducted following our recently published successful recipe developed for studying allosteric inhibitors of BVDV,[28] and Polio-virus helicase.[29] In this case, the pharmacophore requirements derived from the CATALYST analysis reported above, coupled with the indications about the BVDV RdRp residues apparently involved in selected drug-resistant protein mutants (see Section 3), were also considered as input parameters for binding site search. The resulting portion of the enzyme making up the putative binding site interacting with the inhibitors is located in the fingers domain (residues 139–313 and 351–410), consisting of 12 α-helices and 11 β-strands (see Fig. 3A). In BVDV RdRp, as in other viral RdRps, the N terminus of the fingers domain, together with a long insert in the fingers domain (residues 260–288), form the fingertip region that associates with the thumb domain. This region is characterized by a three-strand conformation, and since the fingers and the thumb domains are associated through this fingertip region, the conformational change induced by the RNA template binding into the central channel is somewhat limited. The remainder of the fingers domain is comprised of a β-strand rich region (β-fingers) and an α-helix rich region (α-fingers) close to the palm domain. According to the procedure adopted, all compounds were characterized by a similar docking mode in the putative binding site of the BVDV RdRp, as exemplified by compound **51** in Figure 3.

Importantly, three residues lining the pocket are found to satisfy the pharmacophore hypothesis requirements (see Fig. 3B). The hydrogen bond acceptor (HBA) feature on the inhibitor, represented by the oxygen of the amidic C=O group (see Fig. 1D), localizes hydrogen bond acceptor structures that are in an ideal position

Table 7
Output parameters of the 10 lowest cost hypotheses resulting from the statistical evaluation according to the CATSCRAMBLE validation procedure for the BVDV inhibitors

Hypothesis	ρ	RMDS	Total cost	Hypothesis	ρ	RMDS	Total cost
1	0.835	0.834	129.2	**6**	0.612	0.937	161.3
2	0.821	0.862	141.8	**7**	0.599	0.965	163.5
3	0.782	0.896	143.3	**8**	0.572	0.988	166.9
4	0.644	0.901	154.0	**9**	0.537	1.094	168.1
5	0.619	0.922	157.1	**10**	0.521	1.098	169.9
Hypo1	0.982	0.630	100.1				

Table 8
Mutated residues in **50**^{R}, **51**^{R}, and **53**^{R} BVDV RNA-dependent RNA-polymerase (NBSB RdRp) and relevant concentrations at which the resistant viruses were isolated

Compound	×EC_{50} (μM)	Mutations	Compound	×EC_{50} (μM)	Mutations	Compound	×EC_{50} (μM)	Mutations
50	32×	A392E	**51**	16×	N264D	**53**	32×	I261M, N264D

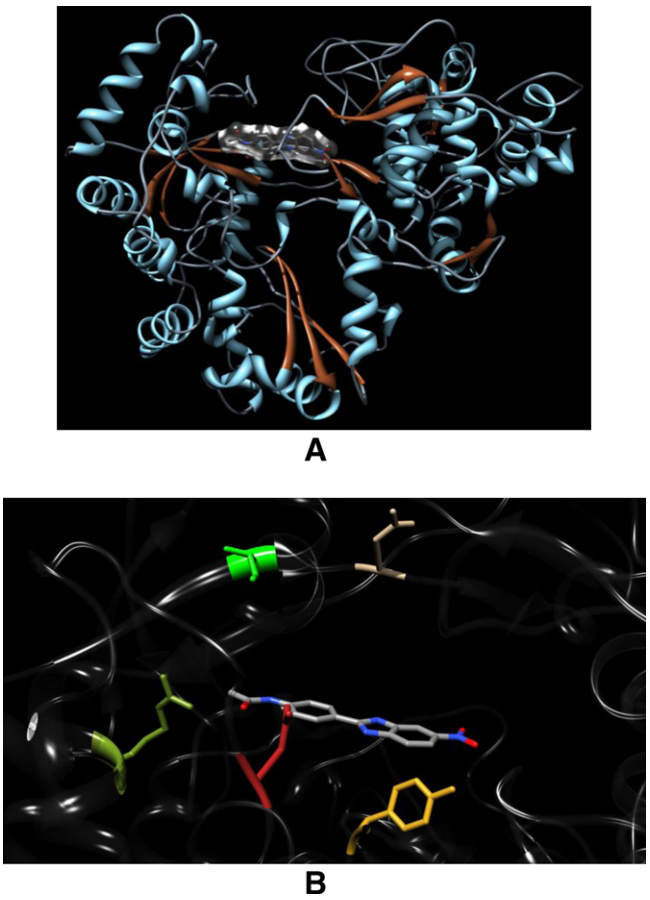

Figure 3. (A) Ribbon diagram of BVDV RdRp/**51** complex structure as resulting from the applied docking procedure. The protein is colored according to its secondary structure: light blue, α-helices; sienna, β-strands, sienna, coils, light gray. The inhibitor **51** is represented as a stick model with carbons in gray, nitrogens in blue, and oxygens in red. The van der Waals surface of **51** is also highlighted in light gray. (B) Details of compound **51** (in a stick representation) in the binding pocket in the enzyme fingers domain. Color scheme as above. The side chains of the three residues satisfying the 3D pharmacophore model requirements for the interaction with compound **51**, and those of the residues involved in resistant mutations, are shown as stick models. The atom color coding is as follows: R295, olive drab; N217, firebrick; Y674, golden rod; I261, green; N264, tan. Hydrogen atoms, counterions, and water molecules are omitted for clarity.

for forming hydrogen bonds with the donor guanidinium group of R295 on the receptor. The **51** hydrogen bond donor feature (HBD), represented by the hydrogen atom on the N1 atom of the azole ring (see Fig. 1D), finds its counterpart in the oxygen atom of the C=O backbone group of N217. The remaining hydrophobic aromatic feature (HYAr) is completed by a π–π stacking interaction of the aromatic rings of **51** and the side chain of Y674 in an edge-on (T-stacking) geometry (see Section 5 for a detailed discussion). Finally, the aminoacids found mutated in BVDV RdRp variants resistant to our series of compounds (Table 8 and Fig. 3B) are also located in closed distance to the inhibitor, and this evidence could ultimately account for the inactivity of these series against viruses expressing these mutated proteins.

5. MM/PBSA drug/protein affinity calculations

A critical issue in docking operations includes the prediction of the correct binding pose and the accurate estimation of the corresponding binding affinity. Despite the enormous size of the conformational space for a given ligand, current docking methodologies have been successfully employed by our group in reproducing crystallographic evidences as well as to predict putative binding modes.[28–30] However, a good scoring function is only a part of the story. Conformational sampling also plays an important role in calculating the binding free energy accurately and efficiently. The conformational flexibility of a given inhibitor and its receptor can be taken into account, according to the procedure adopted in this work, at a hierarchical level, resorting to a wise strategy that employ a rapid and lower level method such as flexible inhibitor/rigid receptor docking at the beginning (Section 4) and turning to the more accurate and quantitative method as the MM/PBSA analysis[31] sampled by molecular dynamics (MD) simulations only once the best pose has been identified and all eventual available criteria have been satisfied.

According to this computational perspective, we performed MM/PBSA calculations for the 33 compounds endowed with activity against BVDV, starting from the corresponding BVDV RdRp/inhibitor complex structures obtained from the docking procedure described in the preceding section. The calculated ΔG_{bind} values for all molecules are listed in Table 9.

Generally speaking, and in harmony with our previous findings,[28–30,33] both the non-bonded mechanical energy components of ΔG_{bind}, ΔE_{VDW} and ΔE_{EL}, afford a substantial, favorable contribution to binding. On the other hand, due the polar character of most compounds, the desolvation penalty paid by these molecules upon binding (ΔG_{PB}) is also quite substantial, so that the net, resulting electrostatic contribution to the affinity of these inhibitors to their enzyme receptor are notably unfavorable. Specifically, for this series of compounds, the mean value of the electrostatic energy ($\Delta E_{EL} + \Delta G_{PB}$) is 32 kcal/mol, whilst the corresponding mean values of the van der Waals and hydrophobic overall interaction energies ($\Delta E_{VDW} + \Delta G_{NP}$) are −52 kcal/mol. Accordingly, it follows that the association between the ligands and the RdRp is mainly driven by more favorable non-polar interactions in the complex than in the solution, in harmony with a proposed general scheme for non-covalent association.[28–30,33]

Considering again the lead compound **51** as a proof-of-principle and going into details, the applications of the MM/PBSA lead to the discovery of further, interesting details about the binding modes of this drug with the residues lining the putative binding site on the surface of the BVDV RdRp (see Fig. 4). In particular, as clearly shown in Figure 4B, the amidic C=O group is engaged in a bifurcated hydrogen bond with the hydrogens of the guanidinium group of R295, characterized by a dynamic average length (ADL) of 2.8 ± 0.2 Å and 2.4 ± 0.1 Å, respectively. This interaction satisfies the first 3D pharmacophore requirement, that is, the HBA feature. A second, stable hydrogen bond takes place between the hydrogen atom on the N1 atom of the inhibitor azole ring and the oxygen atom of the C=O backbone group of N217, with ADL = 2.8 ± 0.2 Å, thus fulfilling the second pharmacophore feature, HBD. Interestingly, during the long MD simulation, the aromatic rings of **51** and the side chain of Y674 are mostly kept seen in an edge-on (T-stacking) geometry. The electronic nature of the π–π interactions indeed favors the stacking of aromatic rings either by parallel-displaced (off-center) or edge-on (T-stacking) geometries, while the face-to-face geometry is unfavorable (particularly in environments where there is a low effective dielectric constant), since the dominant interaction is π-electron repulsion. Accordingly, the third pharmacophore feature (i.e., the hydrophobic aromatic HYAr feature) is also completed by this π–π stacking interaction. Finally, for **51**, the presence of the nitro group as a substituent on the benzimidazole moiety results in a small sub-network of hydrogen bond bridges, involving the two oxygens of $-NO_2$ and the –OH group of Y674 (ADL = 3.2 ± 0.1 Å and 3.6 ± 0.2 Å, respectively), and the same atoms of the inhibitor and the guanidinium group of R529 (ADL = 3.5 ± 0.1 and 3.7 ± 0.2, respectively). The presence of all these stabilizing interactions ac-

Table 9
Free energy components and total binding free energies for compounds of the series A–C on BVDV RdRp

	4	**16**	**18**	**27**	**29**	**30**	**31**	**32**	**33**	**35**	**36**
ΔE_{VDW}	−48.18 (0.15)	−50.36 (0.13)	−50.33 (0.14)	−48.26 (0.14)	−44.27 (0.14)	−44.48 (0.11)	−43.39 (0.13)	−45.44 (0.15)	−46.21 (0.13)	−44.32 (0.12)	−46.26 (0.12)
ΔE_{EL}	−21.67 (0.27)	−22.19 (0.25)	−22.22 (0.25)	−22.48 (0.27)	−19.72 (0.26)	−19.89 (0.26)	−20.30 (0.24)	−21.28 (0.25)	−20.07 (0.30)	−19.39 (0.25)	−19.30 (0.30)
ΔG_{PB}	54.36 (0.21)	58.83 (0.21)	58.32 (0.20)	57.21 (0.22)	49.53 (0.19)	51.66 (0.20)	49.77 (0.20)	51.47 (0.18)	50.32 (0.25)	48.10 (0.21)	50.55 (0.23)
ΔG_{NP}	−4.12 (0.01)	−5.12 (0.00)	−5.21 (0.01)	−4.89 (0.00)	−4.01 (0.01)	−4.35 (0.01)	−4.44 (0.00)	−5.22 (0.01)	−5.33 (0.01)	−5.98 (0.01)	−4.13 (0.00)
$T\Delta S_{solute}$	12.34 (0.88)	13.01 (0.89)	13.56 (0.83)	12.76 (0.72)	12.06 (0.76)	12.37 (0.84)	12.42 (0.79)	13.76 (0.77)	14.06 (0.98)	15.01 (0.88)	12.67 (0.69)
ΔG_{bind}	*−7.27*	*−5.83*	*−5.88*	*−5.66*	*−6.41*	*−4.69*	*−5.94*	*−6.71*	*−7.23*	*−6.58*	*−6.47*
IC_{50}[a]	*4.7*	*53*	*49*	*71*	*20*	*98*	*44*	*12*	*5*	*15*	*18*
	37	**41**	**42**	**203**	**47**	**50**	**51**	**52**	**53**	**54**	**55**
ΔE_{VDW}	−50.02 (0.13)	−46.44 (0.13)	−49.21 (0.14)	−45.61 (0.15)	−45.03 (0.11)	−45.33 (0.13)	−49.06 (0.12)	−45.93 (0.12)	−46.10 (0.13)	−50.00 (0.12)	−50.21 (0.11)
ΔE_{EL}	−20.31 (0.27)	−21.54 (0.25)	−21.47 (0.24)	−21.23 (0.23)	−20.38 (0.26)	−22.55 (0.26)	−22.27 (0.25)	−20.44 (0.24)	−20.59 (0.26)	−20.11 (0.21)	−21.86 (0.28)
ΔG_{PB}	54.14 (0.21)	50.55 (0.22)	54.75 (0.19)	49.85 (0.21)	48.55 (0.20)	51.88 (0.20)	54.23 (0.19)	50.77 (0.18)	51.28 (0.22)	54.22 (0.21)	55.21 (0.22)
ΔG_{NP}	−4.20 (0.01)	−4.77 (0.01)	−4.45 (0.00)	−5.02 (0.01)	−6.03 (0.00)	−4.00 (0.00)	−4.17 (0.00)	−4.71 (0.01)	−4.56 (0.01)	−4.22 (0.00)	−4.36 (0.00)
$T\Delta S_{solute}$	12.21	14.88	12.87	14.39	15.32	12.31	12.63	12.44	12.01	12.56	13.65
ΔG_{bind}	*−8.18*	*7.32*	*−7.51*	*−7.62*	*−7.57*	*−7.69*	*−8.44*	*−7.87*	*−7.96*	*−7.55*	*−7.57*
IC_{50}[a]	*1.0*	*4.3*	*3.1*	*2.6*	*2.8*	*2.3*	*0.65*	*1.7*	*1.5*	*2.9*	*2.8*

	56	**58**	**59**	**62**	**63**	**64**	**66**	**67**	**72**
ΔE_{VDW}	−49.63 (0.13)	−50.01 (0.15)	−42.38 (0l.11)	−48.83 (0.11)	−48.45 (0.12)	−48.36 (0.12)	−50.02 (0.12)	−49.65 (0.13)	−48.05 (0.11)
ΔE_{EL}	−21.92 (0.25)	−22.13 (0.26)	−18.33 (0.26)	−20.46 (0.25)	−20.77 (0.23)	−20.51 (0.23)	−19.47 (0.24)	−20.12 (0.26)	−18.56 (0.23)
ΔG_{PB}	54.82 (0.18)	55.34 (0.18)	47.22 (0.17)	54.13 (0.20)	53.25 (0.19)	52.66 (0.21)	53.89 (0.20)	54.23 (0.20)	50.23 (0.20)
ΔG_{NP}	−4.55 (0.01)	−5.01 (0.00)	−4.29 (0.01)	−5.67 (0.00)	−5.89 (0.01)	−5.97 (0.01)	−5.12 (0.00)	−5.45 (0.00)	−5.66 (0.01)
$T\Delta S_{solute}$	13.78 (0.79)	14.62 (0.85)	12.65 (0.63)	13.99 (0.84)	14.54 (0.79)	14.79 (0.88)	14.01 (0.86)	14.52 (0.90)	14.87 (0.81)
ΔG_{bind}	*−7.50*	*−7.19*	*−5.63*	*−6.84*	*−7.32*	*−7.39*	*−6.71*	*−6.47*	*−7.17*
IC_{50}[a]	*3.2*	*5.4*	*75*	*9.6*	*4.3*	*3.8*	*12*	*18*	*5.5*

All values are in kcal/mol. Errors are given in parenthesis as standard errors of the mean. IC_{50} values are in μM.
[a] IC_{50} values were obtained using the following relationship: $\Delta G_{bind} = RT \ln IC_{50}$.[32]

count for the favorable value of the estimated free energy of binding, ΔG_{bind} = -8.44 kcal/mol (IC_{50} = 0.65 μM), for this inhibitor to the BVDV RdRp, making it the lead compound for this new molecular series.

As the final step in our modeling procedure we decided to model the three compounds for which resistant mutant proteins were identified (i.e., **50**, **51**, and **53**) in the corresponding BVDV RdRp binding site (see Fig. 5A), and to estimate the relevant binding energies. This, with the ultimate goal of testing the ability of the current computational methodology to account for observed drug resistance (see Section 3). Table 10 reports the calculated free energy of binding values and their components for **50**, **51** and **53** in complex with A392E, N264D, and I261M/N264D mutant BVDV RdRps, respectively.

As we can see from this Table, each mutation causes a distinctive energetic change from the wild-type protein. In the case of compound **50**, A392E decreases the net electrostatic component greatly ($\Delta E_{EL} + \Delta G_{PB}$ = +31.24 kcal/mol vs +29.33 kcal/mol for the wild-type RdRp (see Table 9). For compound **51**, N264D causes a substantial decrease in both the electrostatic and van der Waals energies, whilst, for compound **53**, the effect of a conservative substitution (I261 M) slightly mitigate those of N264D. The free energy of binding results listed in Table 10 are fully compatible with the indices of resistance level that were estimated from the experimental EC_{50} values (see Table 8).

A detailed analysis of the interaction of lead compound **51** with the binding site of N264D mutant BDVD RdRp shows that N264 in the wild-type protein has the proton and/or water-mediated interactions with S532 and R157, whereas the corresponding water molecules are missing in the mutant complex MD trajectory (see Fig. 5B and C). In particular, the side chain of N264 makes an hydrogen bond network with the guanidinium group of R159 via water 2134 (ADL = 2.36 ± 0.2 Å and 2.38 ± 0.2 Å, respectively, see Fig. 5B), while the same side chain of R159 is engaged in another water-mediated hydrogen bond (through water 1280) with the side chain –OH moiety of S532 (ADL = 2.41 ± 0.1 Å and 2.35 ± 0.1 Å, respectively, see Fig. 5B). These hydrogen bond mediating water molecules disappear in the respective drug/mutant protein complex, that is, the 264D residue cannot form any hydrogen bond with the R159 residue and this, in turn, cannot interact with the side chain of S532 (see Fig. 5C) This disappearance of the water-mediated hydrogen bond networks allows a slight conformational readjustment of the mutant protein binding site which, in turn, results in a loss of interactions between all residues lining the protein binding pocket and the inhibitor.

One of the most important benchmark in this study, however, is the correspondence between the estimated free energies of binding and the experimental measured EC_{50} values. Indeed, there is a good agreement between the trend exhibited by the IC_{50} values reported in Table 8 and the corresponding biological activity determined for these compounds in BVDV infected cell line (see Tables 2–4). Although we obviously cannot directly compare the computed binding free energy (and hence the corresponding IC_{50}) with the EC_{50} values deriving from experiment, we can observe that, as in our previous experiences,[28–30,33] the rank of the inhibitors with respect to their activity towards its putative target, the RdRp of BVDV, is aptly maintained.

6. Conclusions

In the light of the interesting biological data presented by our new series of 2-phenylbenzimidazoles as selective and potent inhibitors of BVDV replication,[19] in this work we applied a hierarchical combined experimental/molecular modeling strategy to explore the drug leads for the BVDV RNA-dependent RNA-polymerase. Starting from the set of 31 compounds active against the *Pestivirus*, a simple but effective three-dimensional pharmacophore model was developed, characterized by distinct chemical features that may be responsible for the activity of the inhibitors. The pharmacophore generated in this study can be used *per se*, as (1) a three-dimensional query in data base searches to identify compounds with diverse structures that can potentially inhibit BVDV selectively, and, perhaps more importantly from our perspective, (2) to evaluate how well newly designed, second genera-

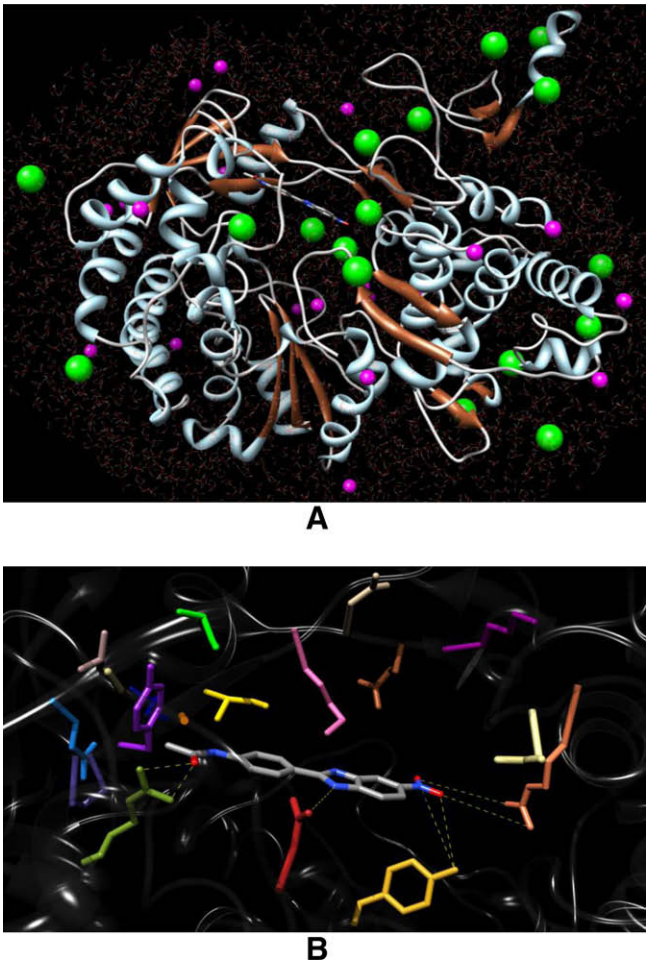

Figure 4. (A) Ribbon diagram of BVDV RdRp/**51** complex structure taken from an equilibrated molecular dynamics snapshot. The protein is colored according to its secondary structure: light blue, α-helices; sienna, β-strands, light gray, coils. The inhibitor **51** is represented as a stick model with carbons in gray, nitrogens in blue, and oxygens in red (hydrogens are not shown). Water molecules are depicted as atom-colored lines. Chlorine and sodium counterions are visualized as green and magenta spheres, respectively (sphere size not in scale for graphical purposes). (B) Details of compound **51** (in a stick representation) in the binding pocket in the enzyme fingers domain. Color scheme as above. The side chains of all residues that form the primary binding pocket interacting with Ascc169 are shown as stick models, and the color coding is the following: N217, firebrick; A221, orange; A222, dark kaki; E258, dodger blue; T259, rosy brown; I261, green; K263, hot pink; N264, tan; E265, sienna; K266, dark magenta; I287, gold; Q288, navy blue; Y289, purple; P290, dark slate blue; E291, pink; R295, olive drab; R529, coral; D531, kaki; Y674, golden rod. Hydrogen bonds are highlighted as light yellow broken lines.

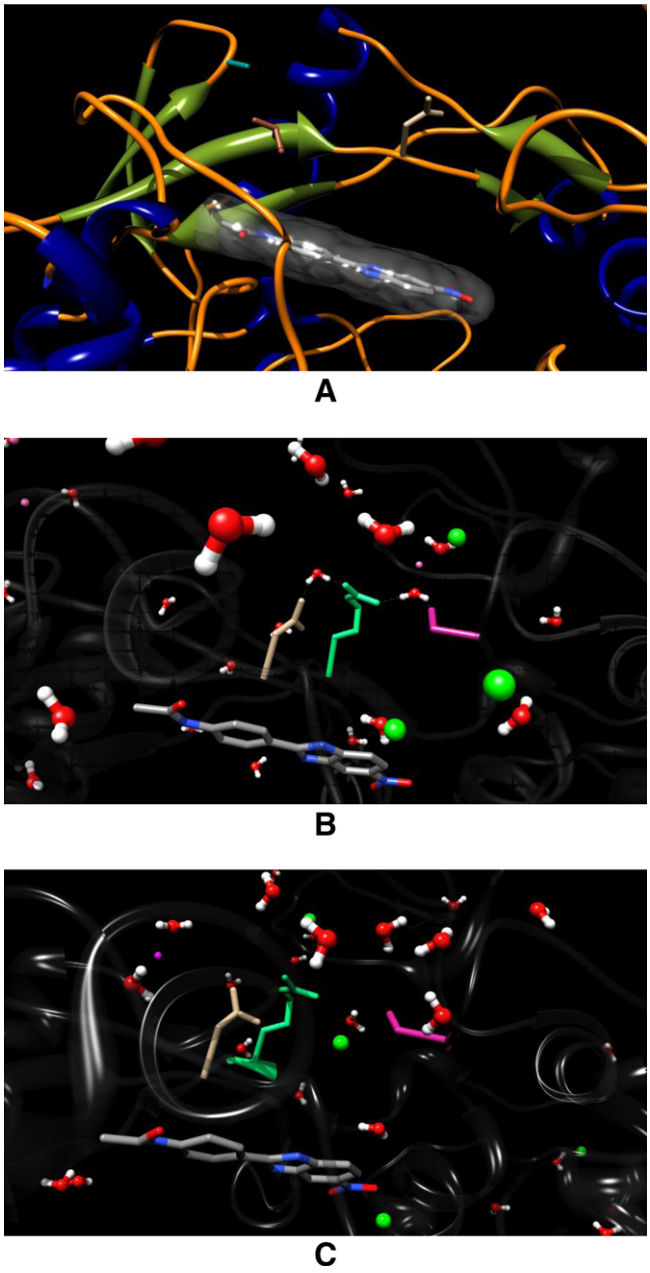

Figure 5. (A) Ribbon diagram of BVDV RdRp/**51** complex structure in which protein residues involved in drug resistance are highlighted. The protein is colored according to its secondary structure: navy blue, α-helices; olive drab, β-strands, orange, coils. The inhibitor **51** is represented as a stick model with carbons in gray, nitrogens in blue, and oxygens in red (hydrogens are not shown); the inhibitor van der Waals surface is sketched as transparent light gray. Water molecules and counterions are omitted. (B) Details of compound **51** (in a stick representation) in the wild-type enzyme binding pocket. The side chains of N264, S532 and R157 are shown as tan, spring green, and violet red sticks, respectively. Water molecules are portrayed as atom-colored sticks-and-balls (red, oxygens, white, hydrogens). Chlorine and sodium counterions are visualized as green and magenta spheres, respectively (sphere size not in scale for graphical purposes). Hydrogen bonds are highlighted as light yellow broken lines. (C) Details of compound **51** (in a stick representation) in the N264D mutant type enzyme binding pocket. The side chains of D264, S532 and R157 are shown as tan, spring green, and violet red sticks, respectively. Water molecules are portrayed as atom-colored sticks-and-balls (red, oxygens, white, hydrogens). Chlorine and sodium counterions are visualized as green and magenta spheres, respectively (sphere size not in scale for graphical purposes).

tion compounds map on the pharmacophore before undertaking any further study, including synthesis.

As a second step, BVDV mutants resistant to lead compounds in our series were isolated, and the mutant residues on the target RdRp were identified.

In a subsequent rigid docking operation, all 31 compounds were placed in a putative binding site on the BVDV RdRp. This step involved a thorough search for a protein binding pocket that could satisfy all the pharmacophore requirements and included the residues found mutated in virus cultures resistant to our molecules.

In the last step, molecular dynamics simulations combined with MM/PBSA calculations were performed on all 31 best docking hits. The calculated free energy of binding between the inhibitors and their target protein showed the same trend of the corresponding experimentally determined EC_{50} values for the entire molecular series. This was an encouraging performance, given that all molecular modeling studies were performed in the absence of any available crystal structure of the protein in complex with an inhibitor. Also, the adopted procedure was able to correctly predict drug binding affinities in the presence of mutated protein residues in-

Table 10
Free energy components and total binding free energies for compounds **50**, **51**, and **53** on resistant mutant BVDV RdRps

	A392E 50	N264D 51	I261M/N264D 53
ΔE_{VDW}	−45.36 (0.15)	−48.39 (0.17)	−45.97 (0.15)
ΔE_{EL}	−22.45 (0.27)	−21.30 (0.25)	−20.01 (0.21)
ΔG_{PB}	53.69 (0.18)	55.01 (0.17)	52.32 (0.18)
ΔG_{NP}	−4.03 (0.00)	−4.2 (0.00)	−4.61 (0.01)
$T\Delta S_{solute}$	12.32 (0.83)	12.44 (0.76)	12.04 (0.79)
ΔG_{bind}	*−5.83*	*−6.44*	*−6.23*
IC_{50}[a]	*53*	*19*	*27*

All values are in kcal/mol. Errors are given in parenthesis as standard errors of the mean. IC_{50} values are in μM.

[a] IC_{50} values were obtained using the following relationship: $\Delta G_{bind} = RT \ln IC_{50}$.[32]

volved in drug resistance. In conclusion, our hierarchical molecular modeling procedure achieved a high reliability, thus constituting an attractive strategy in drug lead exploration. Accordingly, we intend to utilize it to design a new series of more selective and potent BVDV inhibitors.

7. Materials and methods

7.1. Selection of drug-resistant mutants

Drug-resistant variants were selected by serial passages of BVDV in the presence of stepwise doubling drug concentrations, starting from a cell culture infected with an m.o.i. of 0.01, and treated with a drug concentration equal to the EC_{50}. Usually, the amount of virus obtained after each passage was sufficient to determine infection of the next cell culture which, after infection and washing, was incubated with a double amount of the selecting drug. Resistant virus preparations were subjected to RNA extraction, RT-PCR and genome sequencing to identify the mutation patterns responsible for resistance.

7.2. Molecular analysis of resistant viruses

Viral RNAs from wild-type and drug resistant mutants were obtained using the QIAamp viral RNA minikit (QIAGEN), starting from 140 μL of cell-free viral suspensions containing about 106 PFU/mL, in order to determine the nucleotide sequence of the NS3 and NS5B genes of BVDV genome. Reverse transcription reactions were carried out using the Superscript II enzyme (INVITROGEN) and PCR reactions using the Pfx Platinum enzyme (INVITROGEN), following the manufacturer's protocol. Primers used in reverse transcription were RT3 5′-CCCCACAAACCATATCTGATTATTTCTTCTTTA-3′ and RT5B 5′-GTAGATAATCTTGACTACTGTTTAGCTCTTGAG-3′, that bind 360 bp downstream the NS3 gene and 90 bp downstream the NS5B gene, respectively.

The non-structural region containing NS3 gene was amplified by a PCR reaction, carried out with primers A (5′-TAAAAATGCT CATGGTAGGCAACCT-3′) and B (5′-TTATCATTGGGACATGCCTCTTT GA-3′), resulting in a PCR fragment of 2205 bp; PCR amplification consisted of: initial denaturation of 3 min; 34 cycles of denaturation at 94 °C for 30 s, annealing at 56 °C for 30 s and extension at 68 °C for 2.5 min; final extension at 68 °C for 5 min. The non-structural region containing NS5B gene was amplified by two different PCR reactions, carried out, respectively with primers C (ATTATAAAGGAGGTAGGCTCAAGGA) and D (CCATCTGCTGTTATAA CTGGTACTT) and with primers E (5′-ACCCCCTTGTTCAACATCTTTG ATA-3′) and F (5′-GTGGACGGTCCCAACTATATTTATA-3′), resulting into two PCR fragments of 1223 bp and 1792 bp. PCR amplification consisted of: initial denaturation of 3 min; 34 cycles of denaturation at 94 °C for 30 s, annealing at 52.5 °C for 30 s and extension at 68 °C for 2 min; final extension at 68 °C for 5 min.

PCR fragments were purified using the QIAquick PCR Purification kit (QIAGEN) and analyzed using the cycle-sequencing method (CIBIACI service of University of Firenze). Both DNA strands were sequenced with specific primers. The comparative analysis of the chromatograms allowed us to deduce the mutation patterns responsible for resistance.

7.3. Molecular modeling

The entire computational recipe involved the following program packages: CATALYST (v.4.9),[20] AUTODOCK (v. 4.0),[34] AMBER 9.0,[35] MATERIALS STUDIO (v.4.2),[36] INSIGHTII (v.2001),[37] and in-house developed codes (stand-alone and add-on to the commercial software). Molecular graphics images were produced using the UCSF Chimera package (v.1.3).[38] All high-resolution figures were obtained by processing Chimera files with POV-Ray (v.3.6).[39] The extensive, parallel molecular dynamics analyses were performed using 64 processors of the Tartaglia cluster at the University of Trieste (Trieste, Italy), as well as the same number of processors on the IBM/BCX cluster at the CINECA supercomputer center (Bologna, Italy).

7.3.1. Molecular training and test sets selection

For the automated pharmacophore generation with CATALYST, a training set of 22 inhibitors of BVDV RdRp, with EC_{50} values between 0.8 and 89 μM, was defined (Table 5). The test set used for the validation of the pharmacophore model consisted of further 9 derivatives, as reported in Table 6.

7.3.2. Pharmacophore development and mapping

Details of the pharmacophore development procedure with CATALYST have been extensively described in our previous work.[28,40] Briefly, the model structures of all compounds were built using the CATALYST 2D–3D sketcher. Each molecular structure was subjected to energy minimization using the generalized CHARMM force field[41] until the gradient dropped below 0.05. A conformational search was then carried out using the Poling algorithm[42] and the CHARMM force field as implemented in the CATALYST program. The 'best quality' generation option was adopted to select representative conformers over a 0–20 kcal/mol interval above the computed global energy minimum in the conformational space, and the number of conformers generated for each compound was limited to a maximum of 250 as a good compromise between speed and maximum coverage in the conformational space.

Based on the conformations for each compound, the HypoGen module of the CATALYST was used to generate three-dimensional pharmacophore models. During hypotheses generation, the software attempts to minimize a cost function of two main terms: the first penalizes the deviation between the estimated affinities of the training set molecules and their experimental values, whilst the second penalizes the complexity of the hypothesis. The uncertain factor for each compound represents the ratio range of uncertainty in the affinity value based on the expected statistical straggling of biological data collection. Uncertainty influences the first step—also called the constructive phase—of the hypothesis generating process. In this work, an uncertainty of 1.1 was preferred over the default factor of 3.0, as the experimental affinities of our compounds barely span the required four orders of magnitude.

As the CATALYST software can generate pharmacophore hypotheses consisting of a maximum of five hypotheses, an initial analysis revealed that chemical feature types such as hydrogen bond acceptor (HBA), hydrogen bond donor (HBD), hydrophobic aromatic (HYAr), ring aromatic (RA) and positive ionizable (PI) sites could effectively map all critical chemical features of all molecules in

the training and test sets. Accordingly, these five feature types were used to generate 10 pharmacophores from the training set.

The HypoGen module in CATALYST performs two important cost calculations (represented in bit units) that determine the success of any pharmacophore hypothesis. One is called the *fixed cost*, which represents the simplest model that fits all data perfectly, while the second is known as the null cost, and represents the highest cost of a pharmacophore with no features and which estimates activity to be the average of the activity data of the training set molecules. A meaningful pharmacophore hypothesis may result when the difference between these two values is large; for instance, a value of 40–60 bits for a 3D pharmacophore hypothesis may indicate that it has 75–90% probability of correlating the data. Also, the total cost of any pharmacophore hypothesis should be close to the fixed cost to provide any useful model. A further parameter that also determine the quality of a given 3D pharmacophore model with possible predicting value is the *configurational cost*, also known as the *entropy cost* and depends on the complexity of the pharmacophore hypothesis space. For a good hypothesis, this cost, that is the magnitude of the hypothesis space for a given training set of compounds, should be less than 17. If this last cost exceeds 17, there are more degrees of freedom in the training set that the CATALYST algorithm can properly handle and, consequently, the corresponding pharmacophore is likely to be poorly meaningful. Finally, the root-mean-square deviations (RMSDs) and the correlation coefficients ρ represent de facto the quality of the correlation between the estimated and the actual activity data.

7.3.3. Pharmacophore validation

Three validation procedures were followed to determine the statistical relevance and the validity of the proposed 3D pharmacophore models: the test set prediction model, the CATSCRAMBLE method, and the *leave-one-out* procedure. In this work, the former procedure consisted in the collection of further, different compounds into a test set, and in performing a regression analysis by mapping the test set molecules onto the best pharmacophore hypothesis. The high correlation coefficients obtained using the test set compounds revealed the good correlation between the actual and estimated affinities and, hence, the predictive validity of the corresponding 3D hypothesis. The CATSCRAMBLE validation procedure is based on Fisher's randomization test.[22] The goal of this type of validation is to check whether there is a strong correlation between the chemical structures and the biological activity. This is done by randomizing the affinity data associated with the training set compounds, generating pharmacophore hypothesis using the same features and parameters employed to develop the original pharmacophore model. The statistical significance is calculated according to the following formula:

$$\text{significance} = 100 \times [1 - (1 + x/y)]$$

where x is the total number of hypotheses having a total cost lower than the original (best) hypothesis, and y is the total number of HypoGen runs (initial + random runs). Thus, for instance, 49 random spreadsheets (i.e., 49 HypoGen runs) have to be generated to obtain a 98% confidence level. Should any randomized data set result in the generation of a 3D pharmacophore with similar or even better cost values, root-mean-square deviations, and correlation coefficients, then it is likely that the original hypothesis does reflect a chance correlation.

Finally, the *leave-one-out* test checks if the correlation between experimental and computed affinities is heavily dependent on one particular molecule of the training set by re-computing the pharmacophore model with the exclusion of one molecule at a time. Accordingly, 22 new training sets were built, each composed by 21 molecules, and 22 HypoGen calculations were launched under the same conditions. For each run, the hypothesis characterized by the lowest total cost was employed to predict the affinity of the excluded compound and to estimate the new correlation coefficient.

7.3.4. Docking and free energy binding calculations

The optimized structure of the RNA-dependent RNA-polymerase (RdRp) of BVDV were taken from our previous work.[28] The putative binding site for our compounds on the BVDV RdRp was determined using the *ActiveSite_Search* option of the *Binding Site* module of INSIGHTII.[37] *ActiveSite_Search* identifies protein active sites or binding sites by locating cavities in the protein structure. According to the *Site_Search* algorithm employed,[30d] the protein is first mapped onto a grid which covers the complete protein space. The grid points are then defined as free points and protein points. The protein points are grid points, within 2 Å from a hydrogen atom or 2.5 Å from a heavy atom. Then, a cubic eraser moves from the outside of the protein toward the center to remove the free points until the opening is too small for it to move forward. Those free points not reached by the eraser will be defined as site points. After a site is located, it can be modified by expanding or contracting the site. One layer of grid points at the cavity opening site will be added or removed by each expand or contract operation, respectively. Of the three putative binding sites on the surface of the BVDV RdRp discovered by the application of the procedure described above, only one was in the vicinity of the residues found mutated in mutant virus selection. Accordingly, this site was chosen for molecular docking operations.

The model structures of the selected inhibitors were generated using MATERIALS STUDIO (v.4.2).[36] All molecules were subjected to an initial energy minimization, again using the *Sander* module of the AMBER 9 suite of programs,[35] with the *parm99* version of the AMBER force field,[43] with a convergence criterion set to 10^{-4} kcal/(mol Å). A conformational search was carried out using a well-validated, ad hoc developed combined molecular mechanics/molecular dynamics simulated annealing (MDSA) protocol.[28–30,33] Accordingly, the relaxed structures were subjected to five repeated temperature cycles (from 310 to 1000 K and back) using constant volume/constant temperature (NVT) MD conditions. At the end of each annealing cycle, the structures were again energy minimized to converge below 10^{-4} kcal/(mol Å), and only the structures corresponding to the minimum energy were used for further modeling.

The atomic partial charges for the geometrically optimized compounds were obtained using the RESP procedure,[44] and the electrostatic potentials were produced by single-point quantum mechanical calculations at the Hartree–Fock level with a 6-31G* basis set, using the Merz–Singh–Kollman van der Waals parameters.[45] Eventual missing force field parameters for the inhibitor molecules were generated using the *Antech*AMBER module of AMBER 9.0.[33a,35]

The optimized structures of the inhibitors were docked into the BVDV polymerase allosteric binding site by applying a consolidated procedure[28–30,33] based on AUTODOCK 4.0.[34] Following the docking procedure, the structure of all compounds was subjected to cluster analysis with a tolerance of 1 Å for an all-atom root-mean-square (RMS) deviation from a lower-energy structure representing each cluster family. In the absence of any relevant crystallographic information, the structure of each resulting complex characterized by the lowest interaction energy in the prevailing cluster was selected for further evaluation.

Each best substrate/RdRp complex, resulting from the automated docking procedure, was allowed to relax in a 55-Å radius sphere of TIP3P water molecules.[46] The resulting system was minimized with a gradual decrease in the position restraints of the protein atoms. At the end of the relaxation process, all water molecules beyond the first hydration shell (i.e., at a distance >3.5 Å from any protein atom) were removed. Finally, to achieve

electroneutrality, a suitable number of counterions were added, in the positions of the largest electrostatic potential, as determined by the *Leap* module within AMBER 9.0. Given the substantial number of protein/inhibitor complexes, in order to reduce computational time to reasonable limits all protein residues with any atom closer than 20 Å from the center of the mass of each bounded ligand were chosen to be flexible in the dynamic simulations. Subsequently, a spherical TIP3P water cap of radius equal to Å was centered on each inhibitor in the corresponding RdRp complex, including the hydrating water molecules within the sphere resulting from the previous step. After energy minimization of the new water cap for 1500 steps, keeping the protein, the ligand, and the pre-existing waters/ions rigid, followed by a MD equilibration of the entire water/ions sphere with fixed solute for 200 ps, further unfavorable interactions within the structures were relieved by progressively smaller positional restraints on the solute (from 25 to 0 kcal/(mol Å^2)) for a total of 4000 steps. Each system was gradually heated to 310 K at three intervals, allowing a 500 ps interval per each 100 K, and then equilibrated for 2 ns at 310 K, followed by 2 ns of data collection runs, necessary for the estimation of the free energy of binding (vide infra). The MD simulations were performed at constant T = 310 K using the Berendsen et al. coupling algorithm[47] with separate coupling of the solute and solvent to heat, an integration time step of 2 fs, and the applications of the shake algorithm[48] to constrain all bonds to their equilibrium values, thus removing high frequency vibrations. Long-range non-bonded interactions were truncated by using a dual cutoff of 9 and 13 Å, respectively, where energies and forces due to interactions between 9 and 13 Å were updated every 20 time step. The same frequency of update was employed for the non-bonded list. For the calculation of the binding free energy between the RdRp and each compound in water, a total of 200 snapshots were saved during the MD data collection period described above.

The binding free energy ΔG_{bind} of each RdRp/drug complex in water was calculated according to the procedure termed Molecular Mechanic/Poisson–Boltzmann Surface Area (MM/PBSA), and originally proposed by Srinivasan et al.[31] All energetic analyses were performed for a single 2 ns MD trajectory of RdRp/inhibitor complex considered, with 200 unbound protein and drug snapshots taken from the frames in the equilibrated data production phase of that trajectory. The binding free energy for each ligand/receptor system, ΔG_{bind}, was obtained as:

$$\Delta G_{\text{bind}} = \Delta H_{\text{bind}} - T\Delta S_{\text{bind}} \quad (1)$$

$$\Delta H_{\text{bind}} = \Delta E_{\text{MM}} + \Delta G_{\text{solv}} \quad (2)$$

The average values of the enthalpic contribution to ΔG_{bind} were calculated by summing the molecular mechanics energies ($\Delta E_{\text{MM}} = \Delta E_{\text{EL}} + \Delta E_{\text{VDW}}$) and the solvation free energies ($\Delta G_{\text{solv}} = \Delta G_{\text{PB}} + \Delta G_{\text{NP}}$).[49] The polar component of ΔG_{sol} was evaluated using the Poisson–Boltzmann (PB) approach,[50] while the non-polar contribution to the solvation energy was calculated as $\Delta G_{\text{NP}} = \gamma(\text{SASA}) + \beta$, in which γ = 0.00542 kcal/Å^2, β = 0.92 kcal/mol, and SASA is the solvent-accessible surface estimated with the MSMS program.[51] Finally, the last parameter in Eq. (1), that is, the change in solute entropy upon association $-T\Delta S_{\text{bind}}$, was calculated through normal mode analysis. In the first step of this calculation, an 8-Å sphere around the ligand was cut out from an MD snapshot for each ligand–protein complex. This value was shown to be large enough to yield converged mean changes in solute entropy. On the basis of the size-reduced snapshots of the complex, we generated structures of the uncomplexed reactants by removing the atoms of the protein and ligand, respectively. Each of those structures was minimized, using a distance-dependent dielectric constant $\varepsilon = 4r$, to account for solvent screening, and its entropy was calculated using classical statistical formulas and normal mode analysis. To minimize the effects due to different conformations adopted by individual snapshots we averaged the estimation of entropy over 50 snapshots.

References and notes

1. Monath, T. P. *Bull. Soc. Pathol. Exot.* **2006**, *99*, 341.
2. Hayashi, P. H.; Di Bisceglie, A. M. *Med. Clin. North Am.* **2005**, *89*, 371.
3. WHO. Global surveillance and control of hepatitis C. *J. Viral Hepat.* **1999**, *6*, 35.
4. Memon, M. I.; Memon, M. A. *J. Viral Hepat.* **2002**, *9*, 84.
5. Echevarria-Mayo, J. M. *Enferm. Infect. Microbiol. Clin.* **2006**, *24*, 4.
6. Bosch, F. X.; Ribes, J.; Cleries, R.; Diaz, M. *Clin. Liver Dis.* **2005**, *9*, 191.
7. Fried, M. W.; Shiffman, M. L.; Reddy, K. R.; Smith, C.; Marinos, G.; Gonçales, F. L., Jr.; Häussinger, D.; Diago, M.; Carosi, G.; Dhumeax, D.; Craxi, A.; Lin, A.; Hoffman, J.; Yu, J. *N. Eng. J. Med.* **2002**, *347*, 975.
8. Pearlman, B. L. *Am. J. Med.* **2004**, *117*, 344.
9. Huang, Z.; Murray, M. G.; Secrist, J. A. I. I. I. *Antiviral Res.* **2006**, *71*, 351.
10. O'Connor, A. M.; Sorden, S. D.; Apley, M. D. *Am. J. Vet. Res.* **2005**, *66*, 2130.
11. Chase, C. C.; Elmowalid, G.; Yousif, A. A. *Vet. Clin. North Am. Food Anim. Pract.* **2004**, *20*, 95.
12. Houe, H. *Biologicals* **2003**, *31*, 137.
13. Edwards, S.; Fukusho, A.; Lefevre, P. C.; Lipowski, A.; Pejsak, Z.; Roehe, P.; Westergaard, J. *Vet. Microbiol.* **2000**, *73*, 103.
14. Greiser-Wilke, I.; Grummer, B.; Moenning, W. *Biologicals* **2003**, *31*, 113.
15. Buckwold, V. E.; Beer, B. E.; Donis, R. O. *Antiviral Res.* **2004**, *60*, 1.
16. Pietschmann, T.; Bartenschlager, R. *Curr. Opin. Drug Disc. Dev.* **2001**, *4*, 657.
17. (a) Lindenbach, B. D.; Evans, M. J.; Syder, A. J.; Wolk, B.; Tellinghuisen, T. L.; Liu, C. C.; Maruyama, T.; Hynes, R. O.; Burton, D. R.; McKeating, J. A.; Rice, C. M. *Science* **2005**, *309*, 623; (b) Wakita, T.; Pietschmann, T.; Kato, T.; Date, T.; Miyamoto, M.; Zhao, Z.; Murthy, K.; Habermann, A.; Krausslich, H. G.; Mizokami, M.; Bartenschlager, R.; Liang, T. J. *Nat. Med.* **2005**, *11*, 791; (c) Zhong, J.; Gastaminza, P.; Cheng, G.; Kapadia, S.; Kato, T.; Burton, D. R.; Wieland, S. F.; Uprichard, S. L.; Wakita, T.; Chisari, F. V. *Proc. Natl. Acad. Sci. U.S.A.* **2005**, *102*, 9294.
18. (a) Paeshuyse, J.; Leyssen, P.; Mabery, E.; Boddeker, N.; Vrancken, R.; Froeyen, M.; Ansari, I. H.; Dutartre, H.; Rozenski, J.; Gil, L. H. V. G.; Letellier, C.; Lanford, R.; Canard, B.; Koenen, F.; Kerkhofs, P.; Donis, R. O.; Herdewijn, P.; Watson, J.; De Clercq, E.; Puerstinger, G.; Neyts, J. *J. Virol.* **2006**, *80*, 149–160; (b) Puerstinger, G.; Paeshuyse, J.; Herdewijn, P.; Rozenski, J.; De Clercq, E.; Neyts, J. *Bioorg. Med. Chem. Lett.* **2006**, *16*, 5345; (c) Puerstinger, G.; Paeshuyse, J.; Heinrich, S.; Mohr, J.; Schraffl, N.; De Clercq, E.; Neyts, J. *Bioorg. Med. Chem. Lett.* **2007**, *17*, 5111.
19. Tonelli, M.; Simone, M.; Tasso, B.; Novelli, F.; Boido, V.; Sparatore, F.; Paglietti, G.; Pricl, S.; La Colla, P.; Giliberti, G.; Blois, S.; Ibba, C.; Sanna, G.; Loddo, R. *Bioorg. Med. Chem.* **2010**, submitted for publication.
20. CATALYST (v.4.9), Accelrys Inc., San Diego (CA), USA.
21. Sutter, J.; Guner, O. F.; Hoffman, R. D.; Li, H.; Wadman, M. In *Pharmacophore Perception, Development, and Use in Drug Design*; Guner, O. F., Ed.; International University Line: La Jolla, CA, 1999; pp 501–511.
22. Fisher, R. *The Design of Experiments*; Hafner Publishing: New York, NY, USA, 1966.
23. (a) Lai, V. C.; Kao, C. C.; Ferrari, E.; Park, J.; Uss, A. S.; Wright-Minogue, J.; Hong, Z.; Lau, J. Y. *J. Virol.* **1999**, *73*, 10129; (b) Dimitrova, M.; Imbert, I.; Kieny, M. P.; Schuster, C. *J. Virol.* **2003**, *77*, 5401; (c) Piccininni, S.; Varaklioti, A.; Nardelli, M.; Dave, B.; Raney, K. D.; McCarthy, J. E. *J. Biol. Chem.* **2002**, *277*, 45670.
24. Baginski, S. G.; pevear, D. C.; Seipel, M.; Sun, S. C. C.; Benetatos, C. A.; Chunduru, S. K.; Rice, C. M.; Collett, M. S. *Proc. Natl. Acad. Sci. U.S.A.* **2000**, *97*, 7981.
25. Paeshuyse, J.; Leyssen, P.; Mabery, E.; Boddeker, N.; Vrancken, R.; Froeyen, M.; Ansari, I. H.; Dutartre, H.; Rozenski, J.; Gil, L. H. V. G.; Letellier, C.; Lanford, R.; Canard, B.; Koenen, F.; Kerkhofs, P.; Donis, R. O.; Herdewijn, P.; Watson, J.; De Clercq, E.; Puerstinger, G.; Neyts, J. *J. Virol.* **2006**, *80*, 149.
26. Choi, K. H.; Groarke, J. M.; Young, D. C.; Kuhn, R. J.; Smith, J. L.; Pevear, D. C.; Rossmann, M. G. *Proc. Natl. Acad. Sci. U.S.A.* **2004**, *101*, 4425.
27. Choi, K. H.; Gallei, A.; Becher, P.; Rossmann, M. G. *Structure* **2006**, *14*, 1107.
28. Tonelli, M.; Vazzana, I.; Tasso, B.; Boido, V.; Sparatore, F.; Fermeglia, M.; Paneni, M. S.; Posocco, P.; Pricl, S.; La Colla, P.; Ibba, C.; Secci, B.; Collu, G.; Loddo, R. *Bioorg. Med. Chem.* **2009**, *17*, 4425.
29. Carta, A.; Loriga, M.; Paglietti, G.; Ferrone, M.; Fermeglia, M.; Pricl, S.; Sanna, T.; Ibba, C.; La Colla, P.; Loddo, R. *Bioorg. Med. Chem.* **2007**, *15*, 1914.
30. For recent applications of our MDSA protocol see, for instance: (a) Zampieri, D.; Mamolo, M. G.; Laurini, E.; Fermeglia, M.; Posocco, P.; Pricl, S.; Banfi, E.; Scialino, G.; Vio, L. *Bioorg. Med. Chem.* **2009**, *17*, 4693; (b) Mazzei, M.; Nieddu, E.; Miele, M.; Balbi, A.; Ferrone, M.; Fermeglia, M.; Mazzei, M. T.; Pricl, S.; La Colla, P.; Marongiu, F.; Ibba, C.; Loddo, R. *Bioorg. Med. Chem.* **2008**, *16*, 2591; (c) Zampieri, D.; Mamolo, M. G.; Vio, L.; Banfi, E.; Scialino, G.; Fermeglia, M.; Ferrone, M.; Pricl, S. *Bioorg. Med. Chem.* **2007**, *15*, 7444; (d) Carta, A.; Loriga, M.; Piras, S.; Paglietti, G.; Ferrone, M.; Fermeglia, M.; Pricl, S.; La Colla, P.; Collu, G.; Sanna, T.; Loddo, R. *Med. Chem.* **2007**, *3*, 520. and references cited therein.
31. Srinivasan, J.; Cheatham, T. E.; Cieplak, P.; Kollman, P. A.; Case, D. A. *J. Am. Chem. Soc.* **1998**, *120*, 9401.
32. Wang, J.; Morin, P.; Wang, W.; Kollman, P. A. *J. Am. Chem. Soc.* **2001**, *123*, 5221.
33. For a further list of recent applications of the MM/PBSA methodology from our group see, for instance: (a) Pavan, G. M.; Danani, A.; Pricl, S.; Smith, D. K. *J. Am.*

Chem. Soc. **2009**, *131*, 9686; (b) McAuliffe, J. C.; Wang, W. L.; Pavan, G. M.; Pricl, S.; Yang, D.; Chen, S. S.; Lazar, A. J.; Pollock, R. E.; Trent, J. C. *Mol. Oncol.* **2008**, *2*, 161; (c) Negri, T.; Pavan, G. M.; Virdis, E.; Greco, A.; Fermeglia, M.; Sandri, M.; Pricl, S.; Pierotti, M. A.; Pilotti, S.; Tamborini, E. *J. Natl. Cancer Inst.* **2009**, *101*, 194; (d) Ferrone, M.; Perrone, F.; Tamborini, E.; Paneni, M. S.; Fermeglia, M.; Suardi, S.; Pastore, E.; Delia, D.; Pierotti, M. A.; Pricl, S.; Pilotti, S. *Mol. Cancer Ther.* **2006**, *5*, 1467; (e) Tamborini, E.; Pricl, S.; Negri, T.; Lagonigro, M. S.; Miselli, F.; Greco, A.; Gronchi, A.; Casali, P. G.; Ferrone, M.; Fermeglia, M.; Carbone, A.; Pierotti, M. A.; Pilotti, S. *Oncogene* **2006**, *25*, 6140; (f) Pricl, S.; Fermeglia, M.; Ferrone, M.; Tamborini, E. *Mol. Cancer Ther.* **2005**, *4*, 1167; (g) Mamolo, M. G.; Zampieri, D.; Vio, L.; Fermeglia, M.; Ferrone, M.; Pricl, S.; Scialino, G.; Banfi, E. *Bioorg. Med. Chem.* **2005**, *13*, 3797.

34. Huey, R.; Morris, G. M.; Olson, A. J.; Goodsell, D. S. *J. Comput. Chem.* **2007**, *28*, 1145.
35. D. A. Case, T. A. Darden, T. E. Cheatham III, C. L. Simmerling, J. Wang, R. E. Duke, R. Luo, K. M. Merz, D. A. Pearlman, M. Crowley, R. C. Walker, W. Zhang, B. Wang, S. Hayik, A. Roitberg, G. Seabra, K. F. Wong, F. Paesani, X. Wu, S. Brozell, V. Tsui, H. Gohlke, L. Yang, C. Tan, J. Mongan, V. Hornak, G. Cui, P. Beroza, D. H. Mathews, C. Schafmeister, W. S. Ross and P. A. Kollman, AMBER 9, University of California, San Francisco, CA USA, 2006.
36. MATERIALS STUDIO (v.4.2); Accelrys Inc.: San Diego, CA, USA.
37. INSIGHTII (v.2001); Accelrys Inc.: San Diego, CA, USA.
38. (a) Chimera (v.1.3), Resource for Biocomputing, Visualization, and Informatics at the University of California, San Francisco, CA, USA.; (b) Pettersen, E. F.; Goddard, T. D.; Huang, C. C.; Couch, G. S.; Greenblatt, D. M.; Meng, E. C.; Ferrin, T. E. *J. Comput. Chem.* **2004**, *25*, 1605.
39. POV-Ray: Persistence of Vision Raytracer (v. 3.6), Persistence of Vision Pty. Ltd., Williamstown, Victoria, Australia.
40. (a) Zampieri, D.; Mamolo, M. G.; Laurini, E.; Florio, C.; Zanette, C.; Fermeglia, M.; Posocco, P.; Paneni, M. S.; Pricl, S.; Vio, L. *J. Med. Chem.* **2009**, *52*, 5380; (b) Tonelli, M.; Boido, V.; Canu, C.; Sparatore, A.; Sparatore, F.; Paneni, M. S.; Fermeglia, M.; Pricl, S.; La Colla, P.; Casula, L.; Ibba, C.; Collu, D.; Loddo, R. *Bioorg. Med. Chem.* **2008**, *16*, 8447; (c) Di Santo, R.; Fermeglia, M.; Ferrone, M.; Paneni, M. S.; Costi, R.; Artico, M.; Roux, A.; Gabriele, M.; Tardif, K. D.; Siddiqui, A.; Pricl, S. *J. Med. Chem.* **2005**, *48*, 6304.
41. Brooks, B. R.; Bruccoleri, R. E.; Olafson, B. D.; States, D. J.; Swaminathan, S.; Karplus, M. J. *J. Comput. Chem.* **1983**, *4*, 187.
42. (a) Smellie, A.; Teig, S. L.; Towbin, P. *J. Comput. Chem.* **1994**, *16*, 171; (b) Smellie, A.; Kahn, S. D.; Teig, S. L. *J. Chem. Inf. Comput. Sci.* **1995**, *35*, 285; (c) Smellie, A.; Kahn, S. D.; Teig, S. L. *J. Chem. Inf. Comput. Sci.* **1995**, *35*, 295.
43. Wang, J.; Cieplak, P.; Kollman, P. A. *J. Comput. Chem.* **2000**, *21*, 1049.
44. Bayly, C. I.; Cieplak, P.; Cornell, W. D.; Kollman, P. A.; Bayly, C. I.; Cieplak, P.; Cornell, W. D.; Kollman, P. A. *J. Phys. Chem.* **1993**, *97*, 10269.
45. Besler, B. H.; Merz, K. M.; Kollman, P. A. *J. Comput. Chem.* **1990**, *11*, 431.
46. Jorgensen, W. L.; Chandrasekhar, J.; Madura, J. D.; Impey, R. W.; Klein, M. L. *J. Chem. Phys.* **1983**, *79*, 926.
47. Berendsen, H. J. C.; Postma, J. P. M.; Van Gunsteren, W. F.; DiNola, A.; Haak, J. R. *J. Chem. Phys.* **1984**, *81*, 3684.
48. Ryckaert, J. P.; Ciccotti, G.; Berendsen, H. J. C. *J. Comput. Phys.* **1977**, *23*, 327.
49. Jayaram, B.; Sprous, D.; Beveridge, D. L. *J. Phys. Chem.* **1998**, *102*, 9571.
50. Sitkoff, D.; Sharp, K. A.; Honig, B. *J. Phys. Chem.* **1994**, *98*, 1978.
51. Sanner, M. F.; Olson, A. J.; Spehner, J. C. *Biopolymers* **1996**, *38*, 305.